IEEE Photonics Journal
An IEEE Photonics Society Publication

Open Access

Improved Beam Quality of Coherently Combined Angled-Grating Broad-Area Lasers

Volume 5, Number 2, April 2013

Yunsong Zhao
Lin Zhu

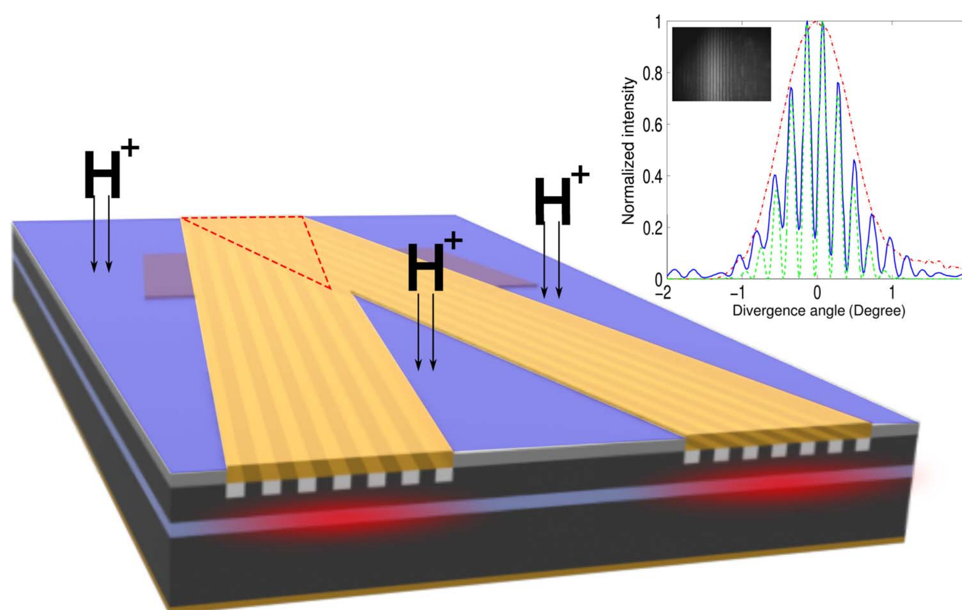

DOI: 10.1109/JPHOT.2013.2245884
1943-0655/$31.00 ©2013 IEEE

IEEE photonics SOCIETY

IEEE

Improved Beam Quality of Coherently Combined Angled-Grating Broad-Area Lasers

Yunsong Zhao and Lin Zhu

Department of Electrical and Computer Engineering, Center for Optical Materials Science and Engineering Technologies, Clemson University, Clemson, SC 29634 USA

DOI: 10.1109/JPHOT.2013.2245884
1943-0655/$31.00 ©2013 IEEE

Manuscript received January 23, 2013; accepted January 31, 2013. Date of publication February 8, 2013; date of current version February 26, 2013. This work was supported in part by an ARO Young Investigator Award under Grant W911NF-11-1-0519, by the DURIP Award under Grant W911NF-11-1-0312, and by a DARPA Young Faculty Award under Grant N66001-10-1-4038. Corresponding author: Y. Zhao (e-mail: yunsonz@g.clemson.edu).

Abstract: We improve the beam quality and performance of coherently combined angled-grating broad-area lasers through current/gain confinement. We show that the nonuniform current/gain distribution in our previous lasers excites the second-order Bragg mode and degrades the beam quality. Ion implantation is used to provide a more uniform current distribution by confining the injected current within the grating area. The far-field measurement result shows that the near-diffraction-limited single-lobe envelope is obtained. Smaller threshold and larger slope efficiency are observed in the L-I curve as well.

Index Terms: Diode lasers, semiconductor lasers.

1. Introduction

Diffraction-limited single-lobe far-field profiles are usually desired for the high-brightness operation of semiconductor lasers. Narrow-ridge waveguide lasers are designed to support a single (waveguide) mode through index guiding to fulfill this requirement. In the large-area lasers for high-power applications, however, weak index guiding is needed for the single-mode operation, and it is not robust against the index perturbation at large pump current. Therefore, special cavity designs are needed to overcome this problem, e.g., unstable resonator lasers [1], angled-grating broad-area lasers [2]–[4], photonic crystal Bragg lasers [5], [6] and slab-coupled optical waveguide lasers (SCOWLs) [7]. These designs could provide over 1-W output power with near-diffraction-limited beam quality in a single emitter. To obtain even higher output power and brightness, beam combining techniques can be used. For those applications where the spectral brightness is not critical, wavelength beam combining can be used to obtain high output power with the brightness similar to a single emitter [8], [9]. High-power diode lasers can also be coherently combined either by the active coherent beam combining, like the master oscillator power amplifier (MOPA) approach [10]–[12] or by the passive coherent beam combining, using common cavities such as Talbot cavity arrays [13], [14] and self-Fourier cavity arrays [15]. However, all these approaches require external optical components and/or precise phase control in the laser arrays. There are few solutions for monolithic coherent beam combining of broad-area lasers. In our recent work, we have reported the first integrated coherent beam combining of angled-grating broad-area lasers [16]. In our demonstration, two angled-grating broad-area lasers are phase locked through Bragg diffraction in an integrated 2-D photonic crystal coupling region. More importantly, our design could be expanded to

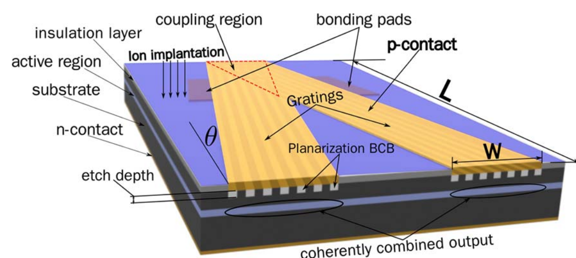

Fig. 1. Schematic plot of the coherently combined angled-grating lasers. L is the length of cavity, W is the width and θ is the tilting angle. The etched gratings are planarized by BCB. The blue area on top represents the ion-implanted region.

a bar-scale coherently combined laser array. However, the far-field profile reported in [16] has an overall double-lobe envelope, and the contrast ratio of the interference fringes is low.

In this paper, we show that the double-lobe envelope of the far-field comes from the second-order Bragg mode. It is excited by the nonuniform current/gain distribution due to the lateral current leakage. Here, we use ion implantation to confine the current in the grating area so that the fundamental Bragg mode will be the preferred lasing mode. We measure the near-field and far-field profiles of the combined laser diodes. The far-field profile has a single-lobe envelope with near-diffraction-limited divergence angle. We compare the measured interference pattern with the theoretically calculated result, and they show good agreement with each other. Compared to our previous result [16], a better contrast ratio of the interference fringes is obtained. We also measure the output light power versus pump current (L-I) curves and spectra. Smaller threshold and larger slope efficiency are observed in the ion-implanted diodes due to better current confinement. Our experimental results have demonstrated that we successfully improve the combined laser beam quality by eliminating the overall double-lobe pattern in the far field.

2. Laser Design and Fabrication

Fig. 1 shows the schematic plot of our coherently combined angled-grating broad-area laser integrated on a single chip. The laser cavity consists of two angled-grating broad-area lasers that tilt to opposite directions and overlap at one facet. The overlapped area defines a 2-D photonic crystal coupling region that coherently combines the two elements through Bragg diffraction. θ is the tilting angle. L and W are the cavity length and output aperture width, respectively. The blue area on top represents the ion-implanted region.

We use a multiple-quantum-well InP wafer to accomplish this paper, and the wafer structure is described in detail in [16]. For fabrication, the gratings are first written on the wafer surface by the e-beam lithography and then transferred into the wafer by dry etching. Before evaporating the metal contacts, the etched gratings are planarized by BCB to prevent metal falling into gratings, and then, the BCB is etched back to expose the unetched p-contact layer. After the p-side metal contact is evaporated, we implant protons in the blue regions shown in Fig. 1. The tilting angle is set to be 10°. We use the first-order gratings with the period of 1.3663 μm corresponding to the wavelength of 1550 nm (the effective index is estimated to be 3.2665). The grating etch depth is about 700 nm. The length of the cavity is about 1.3 mm after cleaving, and the width of a single emitter is about 140 μm corresponding to 100 grating periods. The fabricated diodes are die bonded on C-mounts in the p-side up configuration for measurement.

3. Simulation Results

The planarization material, i.e., BCB, is an electrical isolator. Therefore, the effective resistance of the grating area under the metal contact is larger than that of the p-type highly doped area outside the gratings. As a result, the injected current will concentrate at the edges of the grating area. We carried out a 3-D current distribution simulation in COMSOL for a single emitter. The simulation geometry is shown in Fig. 2. In the simulation model, a grating structure is set on the surface of substrate. All the

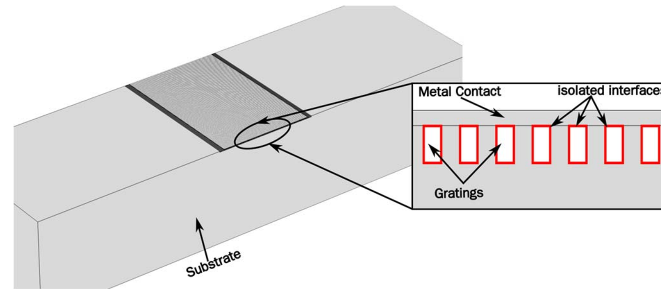

Fig. 2. Simulation geometry in COMSOL. The inset is a zoom-in view around the metal contact. The isolated interfaces are marked in red.

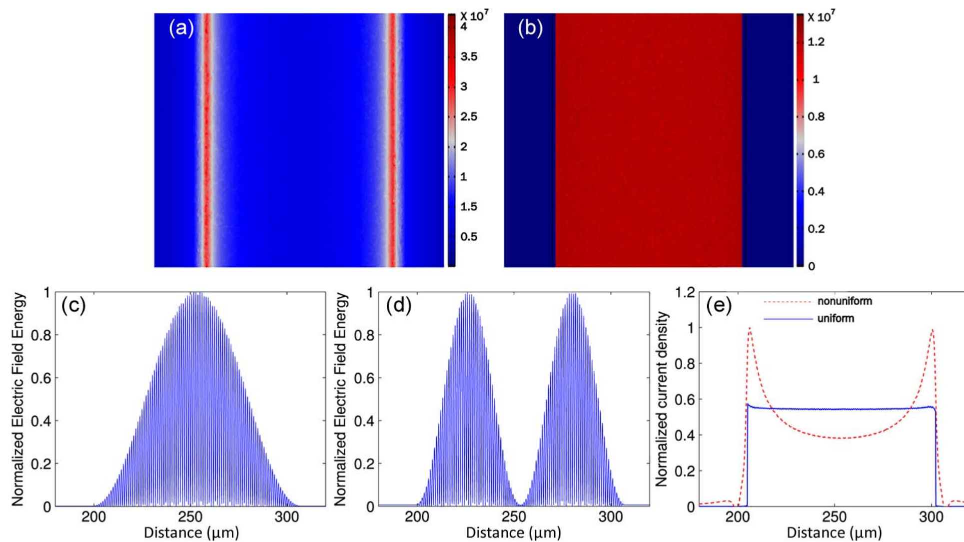

Fig. 3. Simulation results of the injected current distribution. (a) Nonuniform current distribution without ion implantation. (b) The distribution becomes more uniform after increasing the resistance outside the grating area. (c) and (d) Electric fields of the first- and second-order Bragg modes, respectively. (e) Normalized line current density corresponding to (a) in dashed red line and (b) in solid blue line.

interfaces contacting with BCB are set to be electrically isolated, and all the other materials are set to have the same electrical conductivity for simplicity. A gold plate is placed right on the top of the gratings as the metal contact. A current source is set on it. Fig. 3(a) shows the top view of the current density at the position of the quantum-well region.

The result shows a nonuniform current distribution with less current at the center and more current at the edges. We can calculate the modal gain of the first two Bragg modes and show that, with such a nonuniform current distribution, the modal gain of the second-order Bragg mode is actually larger than that of the fundamental mode. We first calculate the mode profiles of the first- and second-order Bragg modes by using the transfer matrix method [17]. They are shown in Fig. 3(c) and (d), respectively. If we denote the modal gain as g_m, it should satisfy

$$\int \mathbb{E}(x)e^{2g(x)\Delta z}dx = \left(\int \mathbb{E}(x)dx\right)e^{2g_m\Delta z} \quad (1)$$

where $\mathbb{E}(x)$ is the electrical field energy, and $g(x)$ is the material gain.

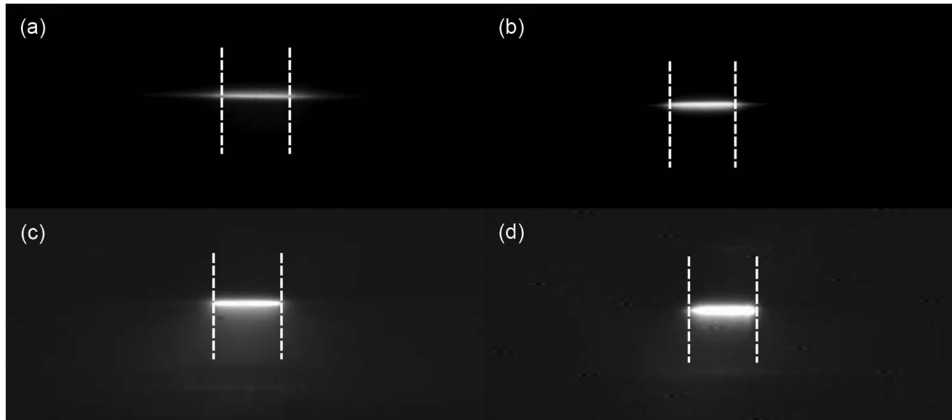

Fig. 4. Near-field images after proton implantation at different energies with the dose of $5 \times 10^{14}/\text{cm}^2$. (a) Not implanted. (b) Ion energy is 180 KeV. (c) Ion energy is 220 KeV. (d) Ion energy is 260 KeV. Between the dashed lines is the emitting aperture.

Therefore, the modal gain can be defined as

$$g_m = \lim_{\Delta z \to 0} \frac{\ln\left(\int \mathbb{E}(x) e^{2g(x)\Delta z} dx\right) - \ln\left(\int \mathbb{E}(x) dx\right)}{2\Delta z} = \frac{\int \mathbb{E}(x) g(x) dx}{\int \mathbb{E}(x) dx}. \tag{2}$$

In the region around threshold, the material gain can be assumed to be linearly proportional to the current density [18]; therefore, we can substitute $g(x)$ in (2) with $J(x)$, which we obtained from the simulation. Obviously, after such substitution, we can only obtain the relative modal gain of different modes, which should be adequate for comparison purpose. We also need to point out that, to make a fair comparison between different current density profiles, we should use the current density profiles obtained with the same current source amplitude. Mathematically, the current density should be normalized as

$$\int J(x) dx = constant \tag{3}$$

where $J(x)$ is the line current density obtained from the simulation result. Fig. 3(e) shows the normalized line current density corresponding to Fig. 3(a) and (b), respectively. Following the steps above, we find the normalized modal gain of the first two Bragg modes with the nonuniform current distribution to be 0.4153 and 0.4498, respectively, The second-order Bragg mode has a larger modal gain than the fundamental mode, which makes it more preferable to be the lasing mode in this situation. To select the fundamental mode, a more uniform current distribution is needed. A practical method to obtain this goal is to increase the resistance of the materials outside of the grating region. Thus, the lateral current leakage is decreased, and the current is confined under the metal contact. The simulation result of the current distribution in this situation is shown in Fig. 3(b), and the normalized modal gains of the first two Bragg modes change to be 0.5311 and 0.5, respectively. Now, with a more uniform current density profile, the fundamental Bragg mode will be preferred as the lasing mode due to a larger modal gain. Experimentally, we can use ion implantation [19], [20] to increase the material resistance outside of the grating region. We first tested several ion-implantation recipes with different ion energies in broad-area lasers. Fig. 4 shows the near-field pictures of different recipes. The near-field images were directly measured by using a near-infrared objective lens and camera, showing the beam profile at the emitting facet. In Fig. 4(a), the nonimplanted device shows obvious tails in the near field. As the ion energy increases, the tails of the emitting aperture become smaller, which indicates less current leakage. As a result, we choose 260-KeV proton with the dose of $5 \times 10^{14}/\text{cm}^2$ as our ion-implantation recipe.

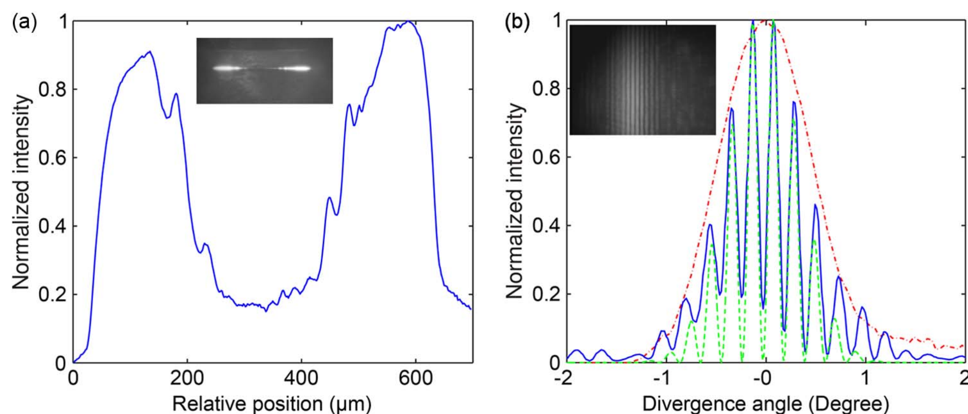

Fig. 5. (a) Near field of the coupled laser. The inset is the camera image. (b) Far field profiles: The blue solid line is the measured far field of the coupled laser, the green dashed line is the calculated far field and the red dash-dot line represents the measured far field of a single angled-grating broad-area laser. We obtain a good agreement between the measured and calculated far field. The inset is the camera image.

4. Measurement Results

We measured the completed laser under CW pump condition in a cryostat with the heat sink temperature set at 230 K. Fig. 5 shows the near-field and far-field measurement results of our laser. In the near field shown in Fig. 5(a), the total width of the emitting aperture is about 160 μm, and the distance between the two apertures is about 425.6 μm. There is about 10% difference in the intensities of the two beams. These values will be used in the theoretical far-field calculation. Compared with the near field reported in Ref. [16], the near-field profile of the ion-implanted lasers has sharper edges of the emitting apertures and larger distinction ratio between the emitting area and dummy area due to better current confinement. In the far field shown in Fig. 5(b), an overall single-lobe envelope is obtained. Multiple fringes in the far field are due to the interference of two coherently combined emitters. The full width at half-maximum (FWHM) is about 1.08°. The angular distance between fringes is about 0.2073°. Compared with our previous far-field result, a much better contrast ratio of the interference fringes is obtained. The difference between peaks and valleys for our previous device is only about 0.2, and in our current device, the difference is improved to be 0.9 in the normalized scale, which indicates better coherence of the two emitters. The reason for better coherence is that, after ion implantation, the first-order Bragg mode becomes the dominant lasing mode and has stronger coupling efficiency.

We also calculate the far-field pattern by applying Fourier transform on the measured near-field profile and compare the calculated result (green dashed line) with the measured far field (blue solid line) in Fig. 5(b). The angular distance between fringes in the calculated result is about 0.2040°. We obtain a good agreement between the two results. Besides, we also show the measured far field of an ion-implanted single angled-grating broad-area laser. It is presented as the red dash-dot line in Fig. 5(b). In [16], the divergence angle of the combined laser is slightly larger than that of the single emitter. For our current lasers, however, the envelope of the far field of the combined laser is almost the same as that of the single emitter, which also suggests better coherence.

At last, the measured L-I curve and spectra are shown in Fig. 6. In the L-I curve, the threshold is found to be about 555 mA, and the slope efficiency is about 0.15 W/A. The strong spontaneous emission is due to the relatively high optical loss of angled-grating cavity before the threshold. The performance is slightly better than our previous device, benefiting from better current confinement. The kinks in the L-I curve are caused by mode hopping, which can be observed in the spectrum measurement shown in Fig. 6(b). When we increase the pump current to about 1200 mA, the peak wavelength suddenly changes from 1546.2 nm to 1550.6 nm. The far-field profile remains the same when the mode hoping happens, so it is only the longitude mode hoping. We believe that the mode

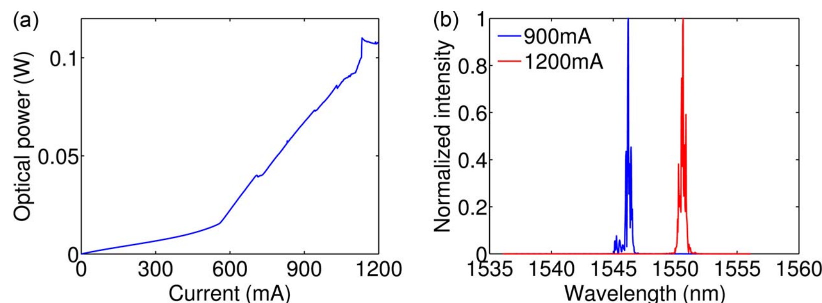

Fig. 6. (a) L-I curve. (b) Spectra at two different pump currents.

hopping is the result of longitudinal mode competition. All the near-field and far-field results were acquired under 1200-mA pump current condition. When we further increase the pump current, the performance of the laser degrades due to the thermal problem.

In summary, the simulation results show that the far-field double-lobe envelope of our previous lasers is due to the second-order Bragg mode. It is excited by the uneven current distribution caused by the lateral current leakage. We use ion implantation to confine the current in the grating area to verify the simulation results. Better beam quality of the coherently combined angled-grating broad-area lasers is successfully obtained with the near-diffraction-limited overall single-lobe far field. The L-I curve measurement also shows smaller threshold and larger slope efficiency because of better current confinement.

Acknowledgment

The authors acknowledge the use of the Gatech Nanotechnology Research Center Facility and associated support services in the completion of this paper.

References

[1] Z. Bao, R. K. Defreez, P. D. Carleson, C. Largent, C. Moeller, and G. C. Dente, "Spatio-spectral characteristics of a high power, high brightness CW InGaAs/AlGaAs unstable resonator semiconductor laser," *Electron. Lett.*, vol. 29, no. 18, pp. 1597–1599, Sep. 1993.

[2] R. J. Lang, K. Dzurko, A. A. Hardy, S. Demars, A. Schoenfelder, and D. F. Welch, "Theory of grating-confined broad-area lasers," *IEEE J. Quantum Electron.*, vol. 34, no. 11, pp. 2196–2210, Nov. 1998.

[3] A. M. Sarangan, M. W. Wright, J. R. Marciante, and D. J. Bossert, "Spectral properties of angled-grating high-power semiconductor lasers," *IEEE J. Quantum Electron.*, vol. 35, no. 8, pp. 1220–1230, Aug. 1999.

[4] K. Paschke, A. Bogatov, F. Bugge, A. E. Drakin, J. Fricke, R. Güther, A. A. Stratonnikov, H. Wenzel, G. Erbert, and G. Tränkle, "Properties of ion-implanted high-power angled-grating distributed-feedback lasers," *IEEE J. Sel. Top. Quantum Electron.*, vol. 9, no. 5, pp. 1172–1178, Sep./Oct. 2003.

[5] L. Zhu, "Photonic crystal Bragg lasers: Design, fabrication, and characterization," Ph.D. dissertation, Caltech, Pasadena, CA, USA, 2008.

[6] L. Zhu, P. Chak, J. K. S. Poon, G. A. Derose, A. Yariv, and A. Scherer, "Electrically-pumped, broad-area, single-mode photonic crystal lasers," *Opt. Exp.*, vol. 15, no. 10, pp. 5966–5975, May 2007.

[7] R. K. Huang, L. J. Missaggia, J. P. Donnelly, C. T. Harris, and G. W. Turner, "High-brightness slab-coupled optical waveguide laser arrays," *IEEE Photon. Technol. Lett.*, vol. 17, no. 5, pp. 959–961, May 2005.

[8] T. Y. Fan, "Laser beam combining for high-power, high-radiance sources," *IEEE J. Sel. Top. Quantum Electron.*, vol. 11, no. 3, pp. 567–577, May/Jun. 2005.

[9] D. Vijayakumar, O. B. Jensen, R. Ostendorf, T. Westphalen, and B. Thestrup, "Spectral beam combining of a 980 nm tapered diode laser bar," *Opt. Exp.*, vol. 18, no. 2, pp. 893–898, Jan. 2010.

[10] L. Goldberg, J. F. Weller, D. Mehuys, D. F. Welch, and D. R. Scifres, "12 W broadarea semiconductor amplifier with diffraction-limited optical output," *Electron. Lett.*, vol. 27, no. 11, pp. 927–929, May 1991.

[11] J. N. Walpole, E. S. Kintzer, S. R. Chinn, C. A. Wang, and L. J. Missaggia, "High-power strained-layer InGaAs/AlGaAs tapered traveling wave amplifier," *Appl. Phys. Lett.*, vol. 61, no. 7, pp. 740–742, Aug. 1992.

[12] S. J. Augst, J. Montoya, K. Creedon, J. Kansky, T. Y. Fan, and A. Sanchez-Rubio, "Intracavity coherent beam combining of 21 semiconductor gain elements using SPGD," presented at the Summaries of Papers Conf. Lasers Electro-Optics (CLEO), San Jose, CA, USA, 2012, Paper CTu1D.1.

[13] R. Waarts, D. Mehuys, D. Nam, D. Welch, W. Streifer, and D. Scifres, "High-power, CW, diffraction-limited, GaAlAs laser diode array in an external Talbot cavity," *Appl. Phys. Lett.*, vol. 58, no. 23, pp. 2586–2588, Jun. 1991.

[14] D. Mehuys, W. Streifer, R. G. Waarts, and D. F. Welch, "Modal analysis of linear Talbot-cavity semiconductor lasers," *Opt. Lett.*, vol. 16, no. 11, pp. 823–825, Jun. 1991.
[15] C. J. Corcoran and K. A. Pasch, "Modal analysis of a self-Fourier laser," *J. Opt. Pure Appl. Opt.*, vol. 7, no. 5, pp. L1–L7, May 2005.
[16] Y. Zhao and L. Zhu, "On-chip coherent combining of angled-grating diode laser toward bar-scale single-mode lasers," *Opt. Exp.*, vol. 20, no. 6, pp. 6375–6384, Mar. 2012.
[17] L. Zhu, A. Scherer, and A. Yariv, "Modal gain analysis of transverse Bragg resonance waveguide lasers with and without transverse defects," *IEEE J. Quantum Electron.*, vol. 43, no. 10, pp. 934–940, Oct. 2007.
[18] A. Yariv and P. Yeh, *Photonics: Optical Electronics in Modern Communications,* 6th ed. Oxford, U.K.: Oxford Univ. Press, 2007.
[19] H. Boudinov, H. H. Tan, and C. Jagadis, "Electrical isolation of n-type and p-type in p layers by proton bombardment," *J. Appl. Phys.*, vol. 89, no. 10, pp. 5343–5347, May 2001.
[20] S. J. Pearton, "Ion implantation for isolation of III-V semiconductors," *Mater. Sci. Rep.*, vol. 4, no. 6, pp. 313–363, 1990.